optica

Observation of second-order meron polarization textures in optical microcavities

Mateusz Król,[1] Helgi Sigurdsson,[2,3] Katarzyna Rechcińska,[1] Przemysław Oliwa,[1]
Krzystof Tyszka,[1] Witold Bardyszewski,[4] Andrzej Opala,[5] Michał Matuszewski,[5]
Przemysław Morawiak,[6] Rafał Mazur,[6] Wiktor Piecek,[6] Przemysław Kula,[7]
Pavlos G. Lagoudakis,[2,3] Barbara Piętka,[1] and Jacek Szczytko[1,*]

[1]Institute of Experimental Physics, Faculty of Physics, University of Warsaw, ul. Pasteura 5, PL-02-093 Warsaw, Poland
[2]Department of Physics and Astronomy, University of Southampton, Southampton SO17 1BJ, UK
[3]Skolkovo Institute of Science and Technology, Moscow, Russian Federation
[4]Institute of Theoretical Physics, Faculty of Physics, University of Warsaw, Warsaw, Poland
[5]Institute of Physics, Polish Academy of Sciences, al. Lotników 32/46, PL-02-668 Warsaw, Poland
[6]Institute of Applied Physics, Military University of Technology, Warsaw, Poland
[7]Institute of Chemistry, Military University of Technology, Warsaw, Poland
*Corresponding author: Jacek.Szczytko@fuw.edu.pl

Multicomponent Bose–Einstein condensates, quantum Hall systems, and chiral magnetic materials display twists and knots in the continuous symmetries of their order parameters known as skyrmions. Originally discovered as solutions to the nonlinear sigma model in quantum field theory, these vectorial excitations are quantified by a topological winding number dictating their interactions and global properties of the host system. Here, we report the experimental observation of a stable individual second-order meron and antimeron appearing in an electromagnetic field. We realize these complex textures by confining light into a liquid-crystal-filled cavity that, through its anisotropic refractive index, provides an adjustable artificial photonic gauge field that couples the cavity photon motion to its polarization, resulting in the formation of these fundamental vectorial vortex states of light. Our observations could help bring topologically robust room-temperature optical vector textures into the field of photonic information processing and storage.

1. INTRODUCTION

Twists in the SO(3) order parameter of magnetic systems lead to topologically protected excitations known as skyrmions, following a concept originating from elementary particle physics [1], which are characterized by nontrivial spin textures [2–5]. Just like quantized singular vortices in superfluid helium or Bose–Einstein condensates, these skyrmionic excitations are topologically robust against external perturbation since they cannot smoothly relax into the defect-free ground state of the system, thus becoming highly important to understand phase transitions and critical behavior in ordered many-body systems down to the quantum level [6]. This robustness has also led to innovative proposals in the field of spintronics of stable information storage and processing with skyrmions at unprecedented spatial scales. They have been observed in chiral magnets [7], non-centrosymmetric magnets [8], surface plasmons [9,10], and exciton–polaritons [11], to name a few, and have reached room-temperature conditions in magnetic thin films [12,13]. Skyrmions, among numerous other topological effects [14], were also observed in liquid crystals (LCs) [15,16].

Skyrmion textures appear as natural excitations in multicomponent quantum systems since a surjective homomorphism links the SU(2) unitary symmetry group to the SO(3) rotational symmetry group. In a photonic system, the two orthogonal polarization components of the electromagnetic field can be described by a three-dimensional Stokes (pseudospin) vector located on the surface of the Poincaré sphere. Therefore, such topological knots and twists in an electromagnetic field can, in principle, exist in the same sense as skyrmions in thin-film magnetic materials. Of special interest are spin textures known as magnetic vortices or "merons," which originate from Yang–Mills theory [17]. Due to their similarity to skyrmions, they are sometimes referred to as half-skyrmions or baby skyrmions since they can possess half of the skyrmion topological integer charge Q defined in a two-dimensional system as

$$Q = \frac{1}{4\pi} \int \mathbf{S} \cdot \left(\partial_x \mathbf{S} \times \partial_y \mathbf{S} \right) \, dx \, dy, \qquad (1)$$

where $\mathbf{S}$ is the order parameter. Alternatively, the charge of the meron can be determined through $Q = vp/2$ from its vorticity
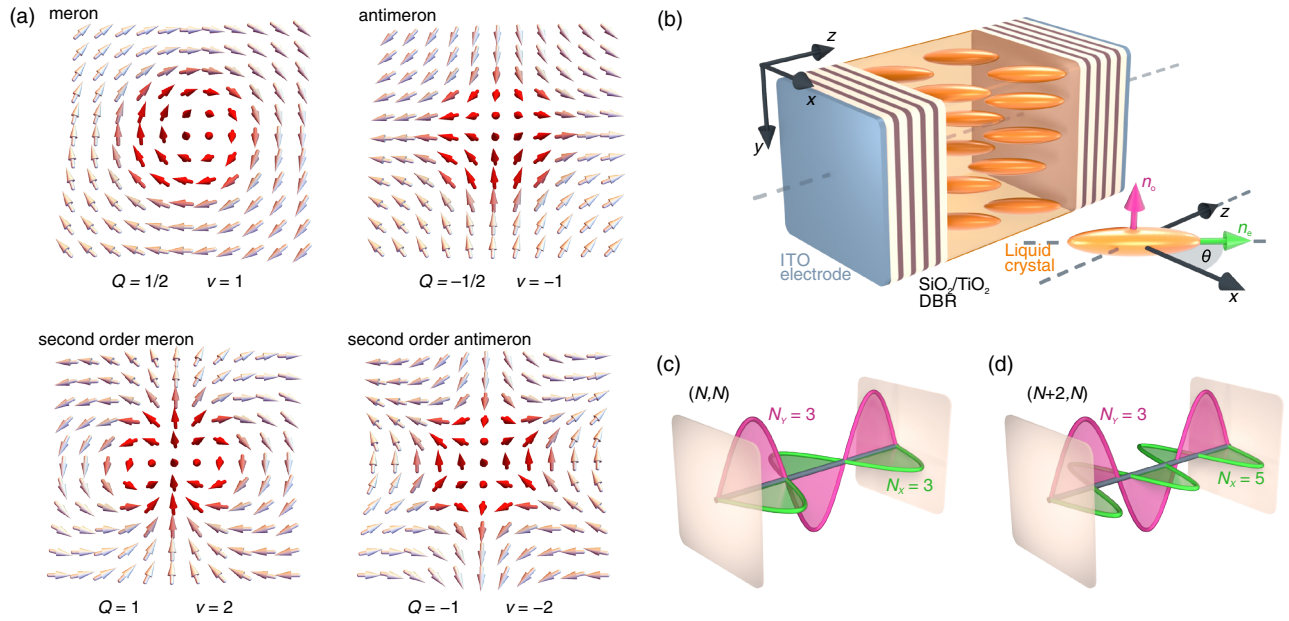
Fig. 1. Meron polarization textures. (a) Illustration of Bloch-type meron, antimeron, second-order meron, and second-order antimeron textures. The arrows represent the order parameter **S** from Eq. (1). (b) Schematic of a microcavity filled with liquid crystal media. The liquid crystal microcavity can be tuned to contain perpendicularly polarized, degenerate modes (c) with the same mode numbers or (d) with different mode numbers. The electric field distribution of X- (Y-) polarized mode is plotted in green (pink) color.

(v) and polarity (p), which describe the in-plane and out-of-plane order parameter orientation, respectively [18]. The simplest configurations are those composed of $v = \pm 1$ and $p = \pm 1$ referred to as merons ($Q = 1/2$) and antimerons ($Q = -1/2$) [Fig. 1(a)], respectively.

In fact, twists in the Hamiltonian parameter space can be regarded as merons whose textures relate to the Berry curvature and charge determines the topological character of condensed matter systems [19–22]. Interestingly, merons cannot exist as isolated objects unless spatially constrained [23,24]. They form either in lattices [25–31] or as paired objects observed before only in magnetic thin films [32].

There also exist higher-order merons, with vorticity $v = \pm 2$, which are referred to as "second-order merons" ($Q = 1$) and "second-order anti-merons" ($Q = -1$) [Fig. 1(a)]. To the best of our knowledge, these second-order twists in order parameter have not been observed in any system to date.

In this study, we present experimental and numerical evidence of second-order merons and antimerons in the photonic field of an optical microcavity filled with a LC at room temperature. The second-order merons appear as the natural eigenmodes of the system due to its tunable optical anisotropic structure. We demonstrate that a pattern of merons (antimerons) can smoothly merge to form a second-order meron (antimeron). Effective Hamiltonians describing the two distinct meron textures are derived linking our observations to alternative low-dimensional condensed matter systems and paving the way towards synthesizing fundamental order parameter twists on nonlinear optical fluids in the strong light–matter coupling regime.

2. RESULTS

We investigated microcavities with a birefringent LC layer enclosed between two parallel distributed Bragg reflectors (DBRs), as schematically shown in Fig. 1(b). The birefringent medium is characterized with two refractive indices: extraordinary n_e, parallel to the director of the LC molecules defining the long optical axis, and ordinary n_o, perpendicular to the director.

This molecular director can be altered by application of external bias to transparent indium tin oxide (ITO) electrodes on the sample. We investigated a configuration in which the director rotates in the $x-z$ plane with applied field. Different effective refractive indices n for linearly polarized light along x and y axes lead to splitting of the optical modes fulfilling the standing wave condition for an optical path length $nd = N\lambda/2$ along the width of the cavity d, for incident wavelength λ and mode number N. In a sufficiently wide cavity, multiple optical modes with different mode numbers can be confined. The unique property of a LC-filled microcavity is the control over the energies of linearly x-polarized optical modes (X) with respect to y-polarized modes (Y), which allows to tune them in and out of resonance with respect to each other. In this work, we concentrate on two different regimes where both X and Y modes have the same parity corresponding to $(N_X, N_Y) = (N, N)$ and $(N_X, N_Y) = (N + 2, N)$ [Figs. 1(c) and 1(d)], which possess uniquely different photonic spin–orbit coupling mechanisms, leading to meron and antimeron textures.

The optical eigenmodes, in the XY polarization basis, can be described by the following Hamiltonian with structure similar to the one describing TE-TM splitting in optically isotropic semiconductor microcavities [33]:

$$\hat{H} = \epsilon(\mathbf{k}) - \left[\delta_x k_x^2 - \delta_y k_y^2 - \Delta E\right]\hat{\sigma}_z - \delta_{xy} k_x k_y \hat{\sigma}_x, \quad (2)$$

where $\epsilon(\mathbf{k}) = \hbar^2(k_x^2/m_x + k_y^2/m_y)/2$ describes cavity photons with masses $m_{x,y}$ along the x, y direction, respectively, δ_x, δ_y, δ_{xy} are parameters proportional to the birefringence $\Delta n = n_e - n_o$ [34], $\hat{\sigma}_{x,y,z}$ are the Pauli matrices, and $\Delta E = E_{Y,N_Y} - E_{X,N_X}$ is the XY mode splitting at normal incidence ($k = 0$). Notably, this splitting is equivalent to the presence of an effective magnetic field

(Zeeman splitting), which plays the role of an artificial photonic gauge field applied to the structure. In this sense, the polarization of the cavity photons plays the same role as a two-level spinor for massive particles. The derivation of Eq. (2) from a simplified model of an optical two-dimensional waveguide filled with an anisotropic dielectric medium is presented in Supplement 1.

In the (N, N) regime, the molecular director is oriented along the z axis, so $\theta = 90°$, and the refractive indices of the cavity medium are the same for normal-incident light polarized along x or y axis (i.e., $m_x = m_y$). Here, we have $\delta_x = \delta_y = \delta_{xy} > 0$ and $\Delta E = 0$, which gives rise to the standard optical spin Hall effect [Figs. 2(a) and 2(b)] observed for microcavity exciton–polaritons and bare cavity photons [35–37]. This unique interplay between photon motion and polarization results in a spatial polarization texture composed of a meron–antimeron lattice, as previously observed in a microcavity exciton–polariton condensate [29].

On the other hand, the $(N + 2, N)$ regime is obtained by changing the molecular director $\theta < 90°$, which tunes the refractive index of the cavity for light polarized along x axis (Fig. 1). In this regime, one has $m_x \neq m_y$, $\delta_x, \delta_{xy} > 0$, $\delta_y < 0$. Detuning the modes slightly, $\Delta E < 0$, leads to severely different artificial spin–orbit coupling of the cavity photons [Figs. 2(c) and 2(d)].

To illustrate the difference between the two regimes, we show in Fig. 3 the real-space polarization textures of light transmitted through a LC microcavity, calculated using the Berreman method [38] (see Supplement 1). Figures 3(a)–3(d) show the adiabatic evolution of the polarization texture in the (N, N) regime for an excitation polarization going from linear to circular. Figure 3(a) shows the previously reported half-skyrmion lattice [29]. Here, four Bloch-type merons of charge $Q = \pm 1/2$—two with positive and two with negative polarity—can be observed in the quadrants of the system. When polarization of the excitation beam changes
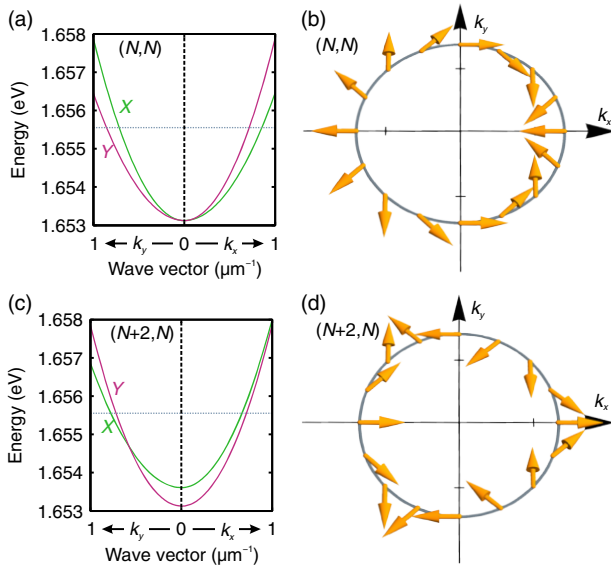

Fig. 2. Spin structure in momentum space. (a) Dispersion relation of cavity modes in (N, N) regime along wave vector in x (k_x) and y (k_y) directions. (b) Polarization at constant energy cross section marked by dashed horizontal line in (a). Polarization state of the inner cavity mode is represented by the Stokes vectors $\mathbf{S} = (S_1, S_2, S_3)$ (yellow arrows). (c) Dispersion relation of cavity modes in $(N + 2, N)$ regime along k_x and k_y. (d) Polarization of the inner cavity mode at constant energy marked by dashed horizontal line in (c) shown by Stokes vectors $\mathbf{S}$.

to elliptical, two merons start merging and create a single second-order meron (also referred to as bimeron) of $Q = +1$ as the laser excitation becomes fully circularly polarized [Fig. 3(d)].

In the $(N + 2, N)$ regime, corresponding to Figs. 3(e)–3(h), a very different behavior is observed. Starting with linearly polarized incident light [Fig. 3(e)], we observe again four antimerons with the same polarity but inverse vorticity compared to the (N, N) regime. When the excitation polarization is gradually changed to circular, two of these antimerons merge, creating one second-order antimeron $Q = -1$, presented in Fig. 3(h).

This dramatic change in the topological integer charge Q of these spin textures is precisely captured by Eq. (2). The charge Q has a different sign between (N, N) and $(N + 2, N)$ regimes because of the polarization structure of parabolic eigenmodes in momentum space (Fig. 2). The splitting between XY modes in both regimes is inverted. The fixed energy of the excitation laser selects an approximate circle in momentum space. Traversing the k-space circle of excited modes results in spin rotation that is in opposite direction between the two regimes.

The real-space polarization textures of the eigenmodes of Eq. (2) can be investigated at room temperature using polarization-resolved imaging of light transmitted through the LC microcavity. The exact polarization state of light can be determined by a measurements of Stokes parameters S_1, S_2, S_3 defined as the degree of linear [S_1 for X (horizontal) and Y (vertical) linear polarizations, S_2 for diagonal and antidiagonal linear polarizations] and circular polarization (S_3). The Stokes parameters corresponding to a second-order meron, given by its analytical form [Eq. (3)], are presented in Figs. 4(a)–4(c). The overlaid black arrows in the S_3 maps correspond to $\mathbf{S}_\| = (S_1, S_2)$. The same symmetry can be observed experimentally in the spatially resolved polarization pattern of circularly polarized light transmitted through the LC microcavity in the (N, N) regime, as shown in Figs. 4(d)–4(f).

Similarly, the analytical pseudospin texture of a second-order antimeron is depicted in Figs. 4(g)–4(i). As expected from numerical modeling, such a polarization texture can be observed in the $(N + 2, N)$ regime. Experimental results, presented in Figs. 4(j)–4(l), reveal second-order antimeron texture. In the case of circularly polarized σ^+ incident light, the LC microcavity, in the $(N + 2, N)$ regime, acts as a full waveplate, and the σ^+ light is transmitted directly, which gives a maximum for S_3 in the center of the incidence spot at $x = y = 0$. Off-center polarization becomes linear far from the center of the topological texture. The rotation of arrows around the center in Figs. 4(d) and 4(j) indicates the rotation of the axis of linear polarization. The difference between the second-order meron [Fig. 4(d)] and antimeron [Fig. 4(j)] is associated with the direction of rotation of the linear polarization axis. Along a clockwise directed path around the center of the light spot, the polarization axis rotates clockwise for a meron and anticlockwise for an antimeron. The difference is clearly visible in the real-space patterns of S_2 depicted in Fig. 4 and reveals exactly the same rotation of polarization in the reciprocal space in Fig. 2. It is straightforward to derive from Eq. (1) that the two opposite vorticities correspond to opposite topological integer charge Q.

Our observations can be interpreted in terms of spin-to-orbital angular momentum conversion [39], which conserves the angular momentum of the excited photons when they convert from one spin to the other through the spin–orbit coupling present in Eq. (2). When a circularly polarized beam excites one spin component it will, in-turn, induce a vortex of winding number 2 in the other
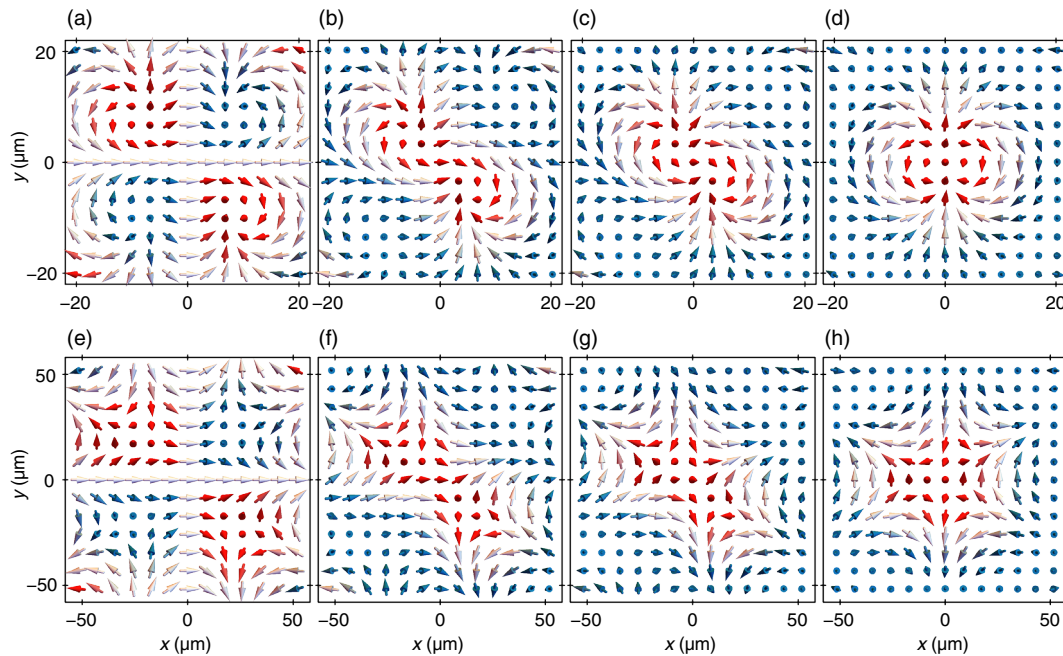
Fig. 3. Spatial meron and antimeron polarization textures in LC microcavities. (a)–(d) Berreman simulations for cavity in (N, N) regime where the arrows represent the Stokes vector $\mathbf{S} = (S_1, S_2, S_3)$ and are colored using the S_3 parameter. The excitation polarization changes smoothly from (a) linear to (d) circular polarization, resulting in merons merging into a second-order meron. (e)–(h) Berreman simulations for cavity in $(N + 2, N)$ regime. The same effect is observed with now two antimerons merging instead to form a second-order antimeron as the excitation polarization changes from linear to circular.
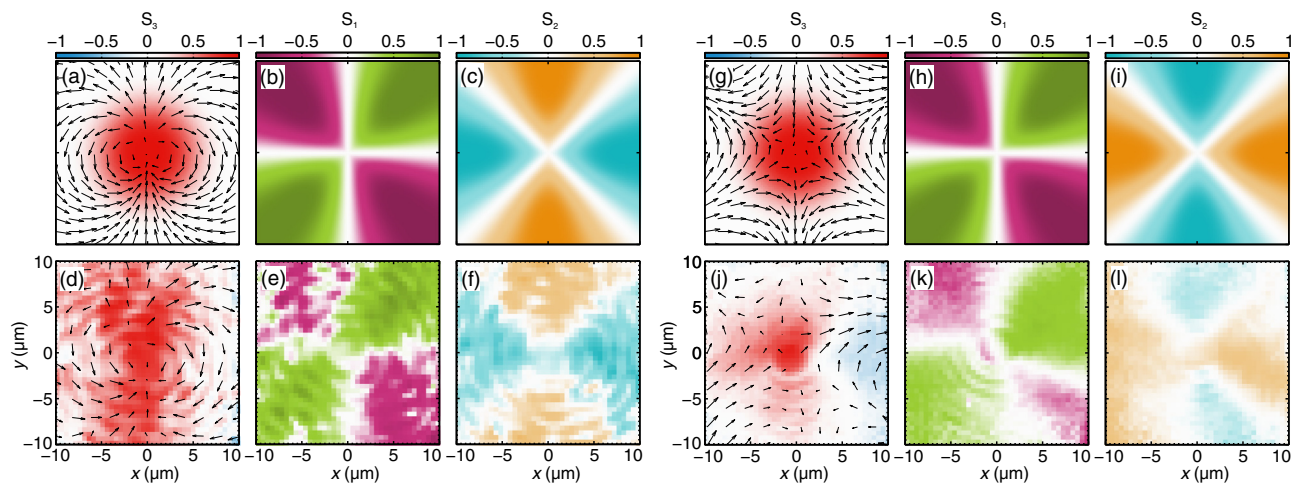

Fig. 4. Second-order meron and antimeron textures in LC microcavities. (a)–(c) S_3, S_1, and S_2 Stokes parameters showing the analytical spin texture of a second-order meron given by Eq. (3). Black arrows correspond to $\mathbf{S}_{\parallel} = (S_1, S_2)$. (d)–(f), Experimental spatial polarization texture of σ^+-polarized light transmitted through a LC microcavity in (N, N) regime. (g)–(i) S_3, S_1, and S_2 Stokes parameters showing the analytical spin texture of a second-order antimeron given by Eq. (3). (j)–(l) Experimental spatial polarization texture of σ^+-polarized light transmitted through a LC microcavity in $(N + 2, N)$ regime.

spin component due to the double-winding nature of the effective spin–orbit coupling magnetic fields [see yellow arrows in Figs. 2(b) and 2(d)] coupling the spins. We point out that both the polarity p (polarization at the core) and winding w (in-plane spin rotation) of the merons are then uniquely determined by the polarization of the excitation beam precisely because of the spin-to-orbital angular momentum conversion between the spin components [39]. For example, in the (N, N) regime, we obtain only a $Q = 1$ second-order meron because the polarity and the winding always have the same sign, regardless of changing the sign of the excitation beam's circular polarization. Conversely, in the $(N + 2, N)$ regime, the

polarity and the winding of the meron are always of the opposite sign, giving a $Q = -1$ second-order antimeron. Finally, the precise size and orientation of the merons depend on the birefringence of the LC filling the cavity and the energy of the optical mode relative to the center of the stopband (see Supplement 1, Fig. S7 and Fig. S8).

3. CONCLUSION

In our study, we have provided the first experimental observation of a second-order meron and antimeron in an electromagnetic field.

The meron and antimeron polarization textures result from the anisotropic refractive index of our optical LC-filled cavity. The artificial photonic gauge field that couples the cavity photon motion with its polarization enables the emergence of vortical polarization patterns. The tunable voltage-dependent orientation of the LC molecules offers a spectrum of different photonic gauge fields that might be difficult to access through engineering of conventional solid state optical microcavities. This flexibility in designing topological spin textures of light can be further combined in optical lattices mimicking magnetic order [40], interference of multiple beams [41], or integrated with photonics devices. Furthermore, our findings are of fundamental interest to other systems described by models hosting analogous textures such as Yang–Mills gauge theory or nonlinear sigma models. These cavity merons can be described as a novel high-order optical vector vortex state, providing a new element of structured light for study in the field of optical physics with potential application in communication and high-resolution imaging [42]. Our work opens new perspectives on using merons as topologically robust optical quaternary memory elements determined by a combination of two orthogonal flows of spin (polarization) vorticity and two opposite orientations of spin polarity. Our system also provides a pathway to study these exotic polarization textures in state-of-the-art nonlinear optical host systems (e.g., annihilation, attraction, and/or repulsion between distinct second-order merons) such as photon or exciton–polariton condensates where they can be generated directly using external laser light and thus of interest to the condensed matter community.

4. METHODS

Skyrmionic textures can be written in polar coordinates as [2]

$$\mathbf{S} = [\cos\Phi(\varphi)\sin\Theta(r), \sin\Phi(\varphi)\sin\Theta(r), \cos\Theta(r)], \quad (3)$$

where $\Phi(\varphi) = v\varphi + \gamma$, with the helicity $\gamma = 0$ or π for Néel-type and $\gamma = \pm\pi/2$ for Bloch-type skyrmion textures. Meron textures in Fig. 1(a) and Figs. 4(a)–4(f) are plotted for $\cos\Theta(r) = 0.5(\cos\pi r + 1)$, where $r \leq 1$.

The polarization of light coming from the cavity is described through the standard definition of the Stokes parameters

$$S_1 = \frac{I_X - I_Y}{I_X + I_Y},$$

$$S_2 = \frac{I_d - I_a}{I_d + I_a},$$

$$S_3 = \frac{I_{\sigma^+} - I_{\sigma^-}}{I_{\sigma^+} + I_{\sigma^-}}. \quad (4)$$

Here, $I_{X,Y}$, $I_{d,a}$, I_{σ^+,σ^-} correspond to the intensities of horizontal, vertical, diagonal, antidiagonal, right-hand circular, and left-hand circular polarized light, respectively.

The Berreman method [38,43] was used to calculate electric the field transmitted at different incidence angles corresponding to varying in-plane wave vectors. The electric field in real space was obtained as a Fourier transform of the results in reciprocal space multiplied with a Gaussian envelope with dispersion $\sigma_x = 0.9\ \mu m$ in real space.

Simulations in Fig. 3 are made for a cavity centered at 750 nm consisting of eight pairs with refractive indices $n_{low} = 1.45$ and

$n_{high} = 2.2$. The cavity is filled with birefringent material with $n_o = 1.539$ and $n_e = 1.939$. The (N, N) regime [Figs. 3(a)–3(d)] is realized at the long optical axis along z direction and the $(N + 2, N)$ regime [Figs. 3(e)–3(h)] for 24.77 deg angle between the director and z axis. Transmission wavelength is equal to 748.9 nm.

A. Experimental Methods

Experimental results were obtained in a polarization-resolved tomography measurement. Light from a broadband halogen lamp was circularly polarized and focused on a given sample with a $100\times$ microscope objective. Transmitted light was collected by a $50\times$ microscope objective, polarization resolved, and focused with a 400 mm lens on a slit of a monochromator equipped with a CCD camera. The full image was obtained by movement of the lens parallel to the slit. Experimental spatial polarization textures present constant energy cross sections around 10 meV above the resonances of the cavities at normal incidence, as shown in Fig. S3 and Fig. S4.

1. (N, N) Sample

Experimental results presented in Figs. 4(d)–4(f) were obtained on a cavity made of DBRs with six pairs of SiO_2/TiO_2 layers designed for maximum reflectance at ≈ 700 nm. The $\approx 2\ \mu m$ thick cavity is filled with birefringent LC with $n_o = 1.504$ and $n_e = 1.801$ with the director oriented along z direction (homeotropic alignment, i.e., with the director perpendicular to the boundary surface). Cavity mode resonance occurs at 768.5 nm. Transmission wavelength is equal to 763.3 nm.

2. (N + 2, N) Sample

Experimental results presented in Figs. 4(j)–4(l) were obtained on a cavity made of DBRs with five pairs of SiO_2/TiO_2 layers designed for maximum reflectance at ≈ 580 nm. The $\approx 2\ \mu m$ thick cavity is filled with birefringent LC with $n_o = 1.539$ and $n_e = 1.949$ with the director oriented along x axis (homogeneous alignment, i.e., with the director parallel to the boundary surface). Experiments were performed with a square waveform with frequency 1 kHz and peak-to-peak amplitude of 1.425 V applied to ITO electrodes that rotate LC molecules towards z axis, resulting in close to degenerate cavity modes in horizontal and vertical polarizations at 583.9 nm and 584.3 nm, respectively. Transmission wavelength is equal to 581.5 nm.

B. Role of Symmetry

The eigenvalue problem for the modes in the birefringent cavity can be analyzed from the point of view of the symmetry. Since we are dealing with the coupling of two modes, we wish to express the relevant Hamiltonians as second-order polynomials in k_x and k_y, with coefficients given by combinations of Pauli matrices. In our considerations, we have to take into account the fact that the transformation law for the Pauli matrices in each case reflects the symmetry of the basis functions under discussion.

(1) In the case of the (N, N) resonance ($\epsilon_{xz} = 0$), the symmetry of the system is given by the group $D_{\infty h}$ with rotation symmetry about the z axis and the reflection plane perpendicular to the z axis.

It is easy to verify that under the reflection in the mirror xy plane, all the Pauli matrices remain invariant, while under the rotation by the angle ϕ about the z axis, only the $\hat{\sigma}_y$ matrix remains invariant, while $(\hat{\sigma}_z \pm i\hat{\sigma}_x) \rightarrow e^{\mp 2i\phi}(\hat{\sigma}_z \pm i\hat{\sigma}_x)$. Taking into account that under this rotation $k_x \pm ik_y \rightarrow e^{\mp i\phi}(k_x \pm ik_y)$ and that the only invariant of second-order is equal to $k_x^2 + k_y^2$, we can postulate the following form of the Hamiltonian:

$$\hat{H} \sim \alpha_0 \hat{\sigma}_y + \alpha_1 \hat{\sigma}_0 + \alpha_2 \hat{\sigma}_y (k_x^2 + k_y^2) + \alpha_3 \hat{\sigma}_0 (k_x^2 + k_y^2)$$

$$+ (\alpha_4 + i\alpha_5)(\hat{\sigma}_z + i\hat{\sigma}_x)(k_x - ik_y)^2$$

$$+ (\alpha_4 - i\alpha_5)(\hat{\sigma}_z - i\hat{\sigma}_x)(k_x + ik_y)^2$$

$$\sim \alpha_0 \hat{\sigma}_y + \alpha_1 \hat{\sigma}_0 + \alpha_2 \hat{\sigma}_y (k_x^2 + k_y^2) + \alpha_3 \hat{\sigma}_0 (k_x^2 + k_y^2)$$

$$+ 2\alpha_4 (\hat{\sigma}_z (k_x^2 - k_y^2) + 2\hat{\sigma}_x k_x k_y)$$

$$- 2\alpha_5 (\hat{\sigma}_x (k_x^2 - k_y^2) - 2\hat{\sigma}_z k_x k_y), \tag{5}$$

with all coefficients α_i real, due to the hermiticity requirement. Under the rotation by π around the x axis, we have $E_x \rightarrow E_x$, $E_y \rightarrow -E_y$, so $\hat{\sigma}_z$ remains invariant, and $\hat{\sigma}_x$ changes sign. Under the same transformation, also the term $k_x k_y$ changes sign, so the term proportional to α_5 is not invariant, and we have to set $\alpha_5 = 0$. Finally, the time reversal symmetry, which in this representation is equivalent to the complex conjugation, requires that $\alpha_0 = \alpha_2 = 0$. If we also set $\alpha_1 = 0$, we obtain the most general form of the Hamiltonian admitted by the symmetry:

$$\hat{H} \sim \alpha_3 \hat{\sigma}_0 (k_x^2 + k_y^2) + 2\alpha_4 (\hat{\sigma}_z (k_x^2 - k_y^2) + \hat{\sigma}_x k_x k_y), \tag{6}$$

with two parameters related to ϵ_{xx} and ϵ_{zz}.

(2) In the case of the $(N + 2, N)$ resonance, $\epsilon_{xz} \neq 0$ and the relevant symmetry group is C_{2h} with the twofold rotation symmetry about the y axis. In this case, $\hat{\sigma}_z$ is invariant under all symmetry operations, while $\hat{\sigma}_x$ and $\hat{\sigma}_y$ change sign under rotation and reflection in the xz plane. The possible invariants are therefore $\hat{\sigma}_0 k_x^2$, $\hat{\sigma}_0 k_y^2$, $\hat{\sigma}_z k_x^2$, $\hat{\sigma}_z k_y^2$, $\hat{\sigma}_x k_x k_y$, and $\hat{\sigma}_y k_x k_y$. However, the last term is excluded due to the time reversal symmetry, so the most general form of the Hamiltonian admitted by the C_{2h} symmetry for a pair of modes of the same parity has six parameters, which can be expressed in terms of n_o, n_e, θ, and mode order N:

$$\hat{H} \sim (\alpha_0 k_x^2 + \alpha_1 k_y^2)\hat{\sigma}_0 + (\Delta E + \alpha_2 k_x^2 + \alpha_3 k_y^2)\hat{\sigma}_z$$

$$+ \alpha_4 k_x k_y \hat{\sigma}_x. \tag{7}$$

Disclosures. The authors declare no conflicts of interest.

Supplemental document. See Supplement 1 for supporting content.

REFERENCES

1. T. H. R. Skyrme, "A unified field theory of mesons and baryons," Nucl. Phys. **31**, 556–569 (1962).

2. N. Nagaosa and Y. Tokura, "Topological properties and dynamics of magnetic skyrmions," Nat. Nanotechnol. **8**, 899–911 (2013).

3. R. Wiesendanger, "Nanoscale magnetic skyrmions in metallic films and multilayers: a new twist for spintronics," Nat. Rev. Mater. **1**, 16044 (2016).

4. S. Krause and R. Wiesendanger, "Skyrmionics gets hot," Nat. Mater. **15**, 493–494 (2016).

5. A. Fert, N. Reyren, and V. Cros, "Magnetic skyrmions: advances in physics and potential applications," Nat. Rev. Mater. **2**, 17031 (2017).

6. V. Lohani, C. Hickey, J. Masell, and A. Rosch, "Quantum skyrmions in frustrated ferromagnets," Phys. Rev. X **9**, 041063 (2019).

7. S. Mühlbauer, B. Binz, F. Jonietz, C. Pfleiderer, A. Rosch, A. Neubauer, R. Georgii, and P. Böni, "Skyrmion lattice in a chiral magnet," Science **323**, 915–919 (2009).

8. L. Peng, R. Takagi, W. Koshibae, K. Shibata, K. Nakajima, T. Arima, N. Nagaosa, S. Seki, X. Yu, and Y. Tokura, "Controlled transformation of skyrmions and antiskyrmions in a non-centrosymmetric magnet," Nat. Nanotechnol. **15**, 181–186 (2020).

9. L. Du, A. Yang, A. V. Zayats, and X. Yuan, "Deep-subwavelength features of photonic skyrmions in a confined electromagnetic field with orbital angular momentum," Nat. Phys. **15**, 650–654 (2019).

10. T. J. Davis, D. Janoschka, P. Dreher, B. Frank, F.-J. M. zu Heringdorf, and H. Giessen, "Ultrafast vector imaging of plasmonic skyrmion dynamics with deep subwavelength resolution," Science **368**, eaba6415 (2020).

11. S. Donati, L. Dominici, G. Dagvadorj, D. Ballarini, M. D. Giorgi, A. Bramati, G. Gigli, Y. G. Rubo, M. H. Szymańska, and D. Sanvitto, "Twist of generalized skyrmions and spin vortices in a polariton superfluid," Proc. Natl. Acad. Sci. USA **113**, 14926–14931 (2016).

12. X. Z. Yu, N. Kanazawa, Y. Onose, K. Kimoto, W. Z. Zhang, S. Ishiwata, Y. Matsui, and Y. Tokura, "Near room-temperature formation of a skyrmion crystal in thin-films of the helimagnet FeGe," Nat. Mater. **10**, 106–109 (2011).

13. S. Woo, K. Litzius, B. Krüger, M.-Y. Im, L. Caretta, K. Richter, M. Mann, A. Krone, R. M. Reeve, M. Weigand, P. Agrawal, I. Lemesh, M.-A. Mawass, P. Fischer, M. Kläui, and G. S. D. Beach, "Observation of room-temperature magnetic skyrmions and their current-driven dynamics in ultrathin metallic ferromagnets," Nat. Mater. **15**, 501–506 (2016).

14. I. I. Smalyukh, "Review: knots and other new topological effects in liquid crystals and colloids," Rep. Prog. Phys. **83**, 106601 (2020).

15. P. J. Ackerman, T. Boyle, and I. I. Smalyukh, "Squirming motion of baby skyrmions in nematic fluids," Nat. Commun. **8**, 673 (2017).

16. D. Foster, C. Kind, P. J. Ackerman, J.-S. B. Tai, M. R. Dennis, and I. I. Smalyukh, "Two-dimensional skyrmion bags in liquid crystals and ferromagnets," Nat. Phys. **15**, 655–659 (2019).

17. M. Shifman, *Instantons in Gauge Theories* (World Scientific, 1994).

18. T. Senthil, A. Vishwanath, L. Balents, S. Sachdev, and M. P. A. Fisher, "Deconfined quantum critical points," Science **303**, 1490–1494 (2004).

19. B. A. Bernevig, T. L. Hughes, and S.-C. Zhang, "Quantum spin Hall effect and topological phase transition in HgTe quantum wells," Science **314**, 1757–1761 (2006).

20. O. Bleu, G. Malpuech, Y. Gao, and D. D. Solnyshkov, "Effective theory of nonadiabatic quantum evolution based on the quantum geometric tensor," Phys. Rev. Lett. **121**, 020401 (2018).

21. A. Gianfrate, O. Bleu, L. Dominici, V. Ardizzone, M. D. Giorgi, D. Ballarini, G. Lerario, K. W. West, L. N. Pfeiffer, D. D. Solnyshkov, D. Sanvitto, and G. Malpuech, "Measurement of the quantum geometric tensor and of the anomalous Hall drift," Nature **578**, 381–385 (2020).

22. C. Guo, M. Xiao, Y. Guo, L. Yuan, and S. Fan, "Meron spin textures in momentum space," Phys. Rev. Lett. **124**, 106103 (2020).

23. T. Shinjo, T. Okuno, R. Hassdorf, K. Shigeto, and T. Ono, "Magnetic vortex core observation in circular dots of permalloy," Science **289**, 930–932 (2000).

24. C. Phatak, A. K. Petford-Long, and O. Heinonen, "Direct observation of unconventional topological spin structure in coupled magnetic discs," Phys. Rev. Lett. **108**, 067205 (2012).

25. H. Flayac, D. D. Solnyshkov, I. A. Shelykh, and G. Malpuech, "Transmutation of skyrmions to half-solitons driven by the nonlinear optical spin Hall effect," Phys. Rev. Lett. **110**, 016404 (2013).

26. D. V. Vishnevsky, H. Flayac, A. V. Nalitov, D. D. Solnyshkov, N. A. Gippius, and G. Malpuech, "Skyrmion formation and optical spin-Hall effect in an expanding coherent cloud of indirect excitons," Phys. Rev. Lett. **110**, 246404 (2013).

27. X. Z. Yu, Y. Tokunaga, Y. Kaneko, W. Z. Zhang, K. Kimoto, Y. Matsui, Y. Taguchi, and Y. Tokura, "Biskyrmion states and their current-driven motion in a layered manganite," Nat. Commun **5**, 3198 (2014).

28. X. Z. Yu, W. Koshibae, Y. Tokunaga, K. Shibata, Y. Taguchi, N. Nagaosa, and Y. Tokura, "Transformation between meron and skyrmion topological spin textures in a chiral magnet," Nature **564**, 95–98 (2018).

29. P. Cilibrizzi, H. Sigurdsson, T. C. H. Liew, H. Ohadi, A. Askitopoulos, S. Brodbeck, C. Schneider, I. A. Shelykh, S. Höfling, J. Ruostekoski, and P. Lagoudakis, "Half-skyrmion spin textures in polariton microcavities," Phys. Rev. B **94**, 045315 (2016).

30. L. Peng, Y. Zhang, W. Wang, M. He, L. Li, B. Ding, J. Li, Y. Sun, X.-G. Zhang, J. Cai, S. Wang, G. Wu, and B. Shen, "Real-space observation of nonvolatile zero-field biskyrmion lattice generation in MnNiGa magnet," Nano Lett. **17**, 7075–7079 (2017).

31. A. Nych, J. Fukuda, U. Ognysta, S. Žumer, and I. Muševič, "Spontaneous formation and dynamics of half-skyrmions in a chiral liquid-crystal film," Nat. Phys. **13**, 1215–1220 (2017).

32. N. Gao, S.-G. Je, M.-Y. Im, J. W. Choi, M. Yang, Q. Li, T. Y. Wang, S. Lee, H.-S. Han, K.-S. Lee, W. Chao, C. Hwang, J. Li, and Z. Q. Qiu, "Creation and annihilation of topological meron pairs in in-plane magnetized films," Nat. Commun. **10**, 5603 (2019).

33. A. Kavokin, G. Malpuech, and M. Glazov, "Optical spin Hall effect," Phys. Rev. Lett. **95**, 136601 (2005).

34. K. Rechcińska, M. Król, R. Mazur, P. Morawiak, R. Mirek, K. Łempicka, W. Bardyszewski, M. Matuszewski, P. Kula, W. Piecek, P. G. Lagoudakis, B. Piętka, and J. Szczytko, "Engineering spin-orbit synthetic Hamiltonians in liquid-crystal optical cavities," Science **366**, 727–730 (2019).

35. C. Leyder, M. Romanelli, J. P. Karr, E. Giacobino, T. C. H. Liew, M. M. Glazov, A. V. Kavokin, G. Malpuech, and A. Bramati, "Observation of the optical spin Hall effect," Nat. Phys. **3**, 628–631 (2007).

36. M. Maragkou, C. E. Richards, T. Ostatnický, A. J. D. Grundy, J. Zajac, M. Hugues, W. Langbein, and P. G. Lagoudakis, "Optical analogue of the spin Hall effect in a photonic cavity," Opt. Lett. **36**, 1095–1097 (2011).

37. K. Lekenta, M. Król, R. Mirek, K. Łempicka, D. Stephan, R. Mazur, P. Morawiak, P. Kula, W. Piecek, P. G. Lagoudakis, B. Piętka, and J. Szczytko, "Tunable optical spin Hall effect in a liquid crystal microcavity," Light Sci. Appl. **7**, 74 (2018).

38. D. W. Berreman, "Optics in stratified and anisotropic media: 4×4-matrix formulation," J. Opt. Soc. Am. **62**, 502–510 (1972).

39. F. Manni, K. G. Lagoudakis, T. K. Paraïso, R. Cerna, Y. Léger, T. C. H. Liew, I. A. Shelykh, A. V. Kavokin, F. Morier-Genoud, and B. Deveaud-Plédran, "Spin-to-orbital angular momentum conversion in semiconductor microcavities," Phys. Rev. B **83**, 241307 (2011).

40. K. Shibata, X. Z. Yu, T. Hara, D. Morikawa, N. Kanazawa, K. Kimoto, S. Ishiwata, Y. Matsui, and Y. Tokura, "Towards control of the size and helicity of skyrmions in helimagnetic alloys by spin–orbit coupling," Nat. Nanotechnol. **8**, 723–728 (2013).

41. T. C. H. Liew, Y. G. Rubo, and A. V. Kavokin, "Generation and dynamics of vortex lattices in coherent exciton-polariton fields," Phys. Rev. Lett. **101**, 187401 (2008).

42. C.-W. Qiu and Y. Yang, "Vortex generation reaches a new plateau," Science **357**, 645 (2017).

43. M. Schubert, "Polarization-dependent optical parameters of arbitrarily anisotropic homogeneous layered systems," Phys. Rev. B **53**, 4265–4274 (1996).